Journal of
Materials Chemistry A

PAPER

View Article Online
View Journal

Check for updates

Cite this: DOI: 10.1039/d5ta10111e

Structural effects of composition tuning in A-site disordered perovskite $La_{0.5}Li_{0.5-x}M_xTiO_3$ (M = Na, K) nanorods for fast interfacial transport for solid composite electrolyte design

Lauren B. Shepard, *[a] Albina Borisevich, [b] Tao Wang, [cd] Ji-young Ock, [c] Alexei P. Sokolov, [cd] X. Chelsea Chen, [c] Sheng Dai [cd] and Susan B. Sinnott *[aefg]

Received 10th December 2025
Accepted 1st March 2026

DOI: 10.1039/d5ta10111e

rsc.li/materials-a

Polymer-ceramic composite electrolytes (CPE) have emerged as promising replacements for currently used liquid organic electrolytes, which pose as safety hazards, in Li-ion batteries. Limits in conductivity enhancement in CPEs is often attributed to a high resistance for Li-ion transport along the interface due to the incompatibility of the polymer and ceramic phases. A clear understanding of the interfacial structure and how this impacts interfacial Li-ion transport is needed in order to efficiently design a CPE with optimal ionic conductivity. In this study, density functional theory (DFT) calculations, in conjunction with scanning transmission electron microscopy (STEM) and electron energy loss spectroscopy (EELS), are used to unveil the bulk and surface structure of $La_{0.5}Li_{0.5-x}M_xTiO_3$ (M = Na, K) (LMTO) nanorods, a newly-reported ceramic system with promising applications in CPEs, and the LMTO interactions with the poly(lithium sulfonyl (trifluoromethane sulfonyl)imide methacrylate) (p(MTFSILi)) polymerized ionic liquid. Substitution of lithium for sodium and potassium onto the A-site perovskite lattice is shown to increase the stability of the preferred pseudocubic perovskite phase because of their increased cation size which allows them to reduce the TiO_6 octahedral rotations in the bulk and at the surface. STEM and EELS results show that LMTO nanorods with differing compositions have Ti-enriched (110)-oriented surfaces. Increased sodium and potassium compositions in LMTO is also shown using the DFT calculations to weaken the binding of the lithium atom to the MTFSI unit when LiMTFSI is adsorbed to the LMTO surface. This weakening of lithium binding to the polymer at the LMTO interface indicates that the lithium mobility is increased, correlating to an increase in interfacial Li-ion transport. Overall, this work provides insights into how to tune the interfacial interactions between the polymer (p(MTFSI)) and ceramic (LMTO) for optimal CPE design.

1. Introduction

With the increasing energy demands of a growing world, the need for safe and high-performing energy storage devices, such as Li-ion batteries, is high. Currently-used Li-ion batteries are composed of liquid organic electrolytes, which have the potential to cause public alarm with reported fires and explosions due to their low electrochemical and thermal stability, toxicity, and flammability.[1–4] As alternatives to liquid organic electrolytes, solid polymer electrolytes (SPEs), ceramic electrolytes, and solid polymer-ceramic composite electrolytes (CPEs) have been proposed.[1,2,5,6] SPEs are good alternatives because of their promising electrochemical and thermal stability, safety, processability, and adhesion to electrodes but, even with significant research progress in the field, they do not yet exhibit ionic conductivity that is sufficiently high.[1,3–5,7]

Li-ion transport in polymers, such as poly(ethylene oxide) (PEO) with dissolved lithium salts, is attributed to the segmental motion of the polymer chain, so the limit in ionic conductivity in polymer electrolytes is attributed to their high glass transition temperatures and semi-crystalline room

---

[a] *Department of Materials Science and Engineering, The Pennsylvania State University, University Park, PA, 16802, USA. E-mail: lzs5735@psu.edu; sbs5563@psu.edu*

[b] *Center for Nanophase Materials Sciences, Oak Ridge National Laboratory, Oak Ridge, TN, 37831, USA*

[c] *Chemical Sciences Division, Oak Ridge National Laboratory, Oak Ridge, TN, 37830, USA*

[d] *Department of Chemistry, Institute for Advanced Materials and Manufacturing, University of Tennessee, Knoxville, TN, 37996, USA*

[e] *Department of Chemistry, The Pennsylvania State University, University Park, PA, 16802, USA*

[f] *Institute for Computational and Data Sciences, The Pennsylvania State University, University Park, PA, 16802, USA*

[g] *Materials Research Institute, The Pennsylvania State University, University Park, PA, 16802, USA*

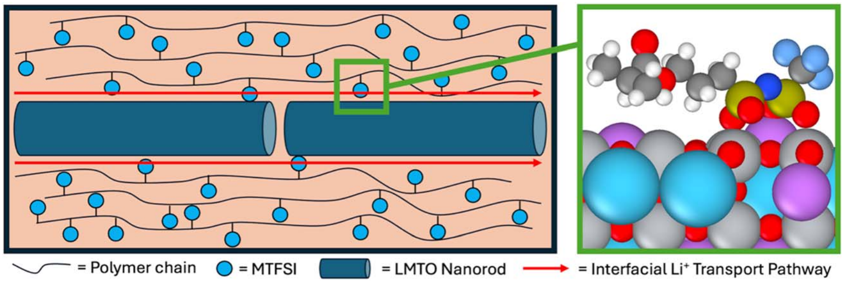

Fig. 1 Schematic showing (left) Li interfacial transport pathway along the aligned LMTO nanorods and (right) the interaction and length scale that DFT calculations can probe.

temperature structure, which restrict polymer chain mobility.[1,3,6] Ceramic electrolytes typically have high room temperature Li-ion conductivities while also maintaining good safety and electrochemical and thermal stabilities.[2,6] Unfortunately, ceramic electrolytes are not ideal for practical applications because of their poor adhesion to electrodes and processability, which is crucial for batteries.[3,6,7] To take advantage of the properties of both SPEs and ceramics, CPEs were developed, and some have been shown to have high ionic conductivity properties and mechanical strength while also having good stability, safety, and adhesion to electrodes.[2,5–7]

In CPEs, a ceramic, inorganic filler is added to the polymer matrix. The addition of the ceramic filler reduces polymer crystallization and helps increase the segmental dynamics of the polymer chains, thus increasing the ionic conductivity.[6] This inorganic filler can either be active with a room temperature Li-ion conductivity higher than the polymer, or inert with no significant Li-ion conductivity.[3,5–8] When the inert ceramic and polymer phases are combined in the CPE, there are two pathways for ions to transport through the system: (i) through the bulk polymer phase only and (ii) in the polymer interfacial layer along the polymer-ceramic interface.[3,6,7,9] When an active ceramic filler is used, an additional pathway mostly through the ceramic particles is possible; however, we have shown that whether this mechanism is present is critically dependent on the value of the polymer-ceramic interface ion exchange time.[3,6,7,10] Two of the pathways, through the bulk ceramic phase and through the bulk polymer phase only, are well studied, while the kinetics and mechanisms of interfacial ion transport is mostly unknown and yet to be elucidated.[6,7] For most CPEs where the volume fraction of the ceramic filler, whether active or inert, is lower than that of the polymer (termed "ceramic-in-polymer"), the major conduction pathway is through the polymer matrix, suggesting that the ion conduction mechanisms are through the polymer and along the interface and thus the bulk ionic conductivity of the ceramic filler does not contribute to conductivity enhancement.[2,6,7,11] Consequently, limitations in conductivity enhancement compared to the corresponding SPE in the composites is attributed to high interfacial resistance to transport along the polymer interfacial layer.[2,6,7,11–13]

High interfacial resistance to ion transport originates from the incompatibility and adherence of the polymer and ceramic components, which negatively impacts ionic conductivity in many CPEs.[6] This means that understanding and tuning interfacial polymer/ceramic electrostatic interactions and ion transport along and across the interface is key to designing a high performing CPE. We know from models, such as the Anderson-Stuart model developed for silicate glasses, that for small ions, such as lithium, electrostatic interactions are the main contribution to the activation barrier for ion transport in polymer electrolytes.[14] The importance of electrostatic interactions transfers from polymer electrolytes to composite electrolytes, especially for reducing activation barrier and therefore enhancing ion transport both in the bulk polymer and along the polymer-ceramic interface. Because of the complexity of the interfacial structure and the limitations in experimental techniques that can probe and analyze the interfacial processes, there are few methodical studies to design and understand the polymer-ceramic interface in literature, with most studies utilizing a screening method with sporadic choices of polymer and ceramic components.[6,7]

The use of computational methods, such as density functional theory (DFT), alongside experimental synthesis and testing allows for a deeper understanding of the CPE structure and transport mechanisms. In DFT calculations, which are electronic-scale, quantum-mechanics based calculations, the system is constrained to a few hundred atoms. Due to the size restrictions of DFT, the polymer phase is represented by a monomer unit, which we term a polymer fragment for the purposes of this work, and is added to the ceramic slab as an absorbate. While this representation of the CPE surface removes any of the segmental dynamics of the polymer which are important for ion transport, these calculations provide valuable information regarding the electrostatic interactions at the interface which play a key role in ion transport at the nanometer scale, specifically at the polymer-ceramic interface, as seen in Fig. 1. DFT calculations are also static at absolute zero, meaning static properties, such as adsorption energy and lithium binding energies, are being calculated to subsequently lend insight into kinetic properties.

In previous work, DFT calculations were used to correlate adsorption energy (E_{ads}) and lithium binding energy ($E_{\mathrm{bind}}^{\mathrm{Li}}$) to experimentally obtained ionic conductivity measurements for dual-ion conducting (DIC) poly(ethylene oxide) (PEO) – based CPEs with lithium bis(trifluoromethane sulfonyl)imide (LiTFSI) salt and either $\mathrm{Al_2O_3}$, perovskite $\mathrm{La_{0.8}Sr_{0.2}Ga_{0.8}Mg_{0.2}O_{2.55}}$ (LSGM), or fluorite $\mathrm{Gd_{0.1}Ce_{0.9}O_{1.95}}$ (GDC) as the ceramic filler.[15] Specifically, a more negative adsorption energy, corresponding to more favorable surface interactions between the LiTFSI and ceramic slab, was found to correlate with a less negative lithium binding energy, meaning the lithium atom is less strongly bound to the TFSI anion.[15] Therefore, for a calculation of a LiTFSI molecule with either a Al_2O_3, GDC, or LSGM slab, static DFT calculations were able to accurately explain experimental kinetic properties, ultimately showing that enhanced surface adsorption interactions between the phases can help to enhance lithium transport in DIC CPEs, where the anion and cation are both mobile.[15]

In our previous work, a flux synthesis method was reported, allowing for the synthesis of A-site disordered cubic ($Pm\bar{3}m$) or pseudocubic ($P4/mmm$) perovskite $La_{0.5}Li_{0.5-x}M_xTiO_3$, M = Na, K, (LMTO) nanorods with high surface area.[16] The development of the flux synthesis method solved one of the long-standing issues of synthesizing a cubic or pseudocubic perovskite phase LLTO, which is a commonly used superionic ceramic filler.[3,8,16] The cubic or pseudocubic perovskite phase is preferred for ionic conductivity properties because it has a more disordered distribution of lithium, lanthanum, and vacancies (if any) than other lower-symmetry perovskite polymorphs, such as the layered tetragonal ($P4/mmm$) and orthorhombic phases ($Pnma$), for example.[8,17] It should be noted here that, in our previous work, Rietveld refinement of XRD data for LMTO nanorods showed equally good fits of both the cubic and pseudocubic perovskite phase.[16] The pseudocubic phase ($P4/mmm$) is very nearly cubic ($Pm\bar{3}m$), with slight distortions in one dimension of the crystal lattice due to octahedral distortions slightly lowering the symmetry of the crystal structure.[18] Ionic radii differences between the Li^+, Na^+, K^+, and La^{3+} cations on the cation suggest that the crystal should be slightly distorted from cubic phase and favor the pseudocubic phase.

Because of the flux synthesis medium used to make the nanorods, it was found that sodium and potassium atoms also uniformly occupied the A-site alongside lanthanum and lithium.[16] This was determined through energy dispersive X-ray spectroscopy (EDS) measurements, which showed a uniform distribution of Na, K, and La across the bulk LMTO nanorod, and XRD refinement.[16] LLTO is an A-site superionic perovskite, but, in this work, the A-site vacancies were mostly filled to allow for the controlled study of the ion transport mechanism along the interface.[9,16] Tolerance factor calculations were reported to show that the addition of sodium and potassium on the A-site lattice can help stabilize the cubic or pseudocubic perovskite LMTO phase due to the larger ionic radii of the sodium and potassium ions at XII coordination.[16] It is important to note that, while the tolerance factor is a good predictor for perovskite phase, synthesis conditions such as thermal history can lead to LLTO samples with similar compositions adopting different crystal structures.[17,19–23] When $Li_{0.11}Na_{0.24}K_{0.02}La_{0.43}TiO_{2.82}$ nanorods (LMTO-800) were combined with a single-ion conducting (SIC) copolymer formed with vinyl ethylene carbonate (VEC) and lithium sulfonyl (trifluoromethane sulfonyl)imide methacrylate (LiMTFSI), the subsequent CPE with 50 wt% LMTO had a room temperature bulk conductivity of 3.0×10^{-5} S cm^{-1}, an approximate two-fold enhancement compared to the corresponding SIC SPE which has a bulk room temperature conductivity of 1.4×10^{-5} S cm^{-1}.[9,16] CPEs with commercially-available LLTO were also analyzed and showed no conductivity enhancement.[9,16] In further work and characterization of these LMTO and LiMTFSI based CPEs, the enhancement in conductivity was attributed to the formation of a percolating interfacial polymer layer, which facilitates faster lithium-ion transport by mitigating ion–ion correlations, approximately 5 nm thick around the LMTO nanorods. The nanorod morphology, with a small average diameter (~33 nm) and high aspect ratio (~5), is advantageous for CPE applications because the nanorods can align to form a continuous interfacial transport pathway for ions, as seen in Fig. 1.[2,3,9,16,24] Li tracer exchange nuclear magnetic resonance (NMR) spectroscopy for the LMTO and LiMTFSI based CPEs confirmed that LMTO acts as an inert ceramic filler, with no exchange of lithium ions between the polymer and ceramic phases seen even at long timescales.[9,10] Therefore, electrochemical measurements in conjunction with NMR measurements of the LMTO-based CPE revealed that the enhancement in conductivity is attributed to an increase in interfacial ion transport.[9,10] It was suggested that the addition of sodium and potassium ions in LMTO could enhance the interfacial lithium-ion transport mechanism, but no direct proof was reported.[16] This could suggest that tailoring the A-site composition of the LMTO nanorod can help to tune LMTO surface interactions with the polymer, helping to enhance interfacial Li-ion transport and consequently the total ionic conductivity of the CPE.

Here, we use DFT calculations to evaluate the impact that the LMTO structure has on phase stability and interactions between the ceramic surface and p(LiMTFSI) polymer. First, bulk LMTO calculations of pseudocubic and orthorhombic perovskite phases show that the decomposition enthalpy gap between the phases is reduced with increasing sodium and potassium content. Structurally, Ti–O and La–O bond length distributions narrow and the octahedral TiO_6 rotations reduces, with the average TiO_6 octahedral rotation angle decreasing (trending towards fully symmetric and cubic) with increasing sodium and potassium content. As previously reported, this can be attributed to the increased sodium and potassium ion size, allowing them to more stably occupy the large A-site. Our High Angle Annular Dark Field (HAADF) Scanning Transmission Electron Microscopy (STEM) and Electron Energy Loss Spectroscopy (EELS) results then probed the LMTO nanorod surface to reveal their (110)-oriented and Ti-rich surface chemistry, which was shown to not change with LMTO composition. These surface chemistry studies then informed the modeling, where DFT calculations of Ti-terminated and (100)-oriented LMTO slabs showed that the electrostatic interactions between LMTO and MTFSI increase with sodium and potassium composition. This indicates that the surface with sodium and potassium is more energetically stable and has stronger interactions with the polymer, leading to a reduced binding of lithium to the anion unit and thus increased mobility of lithium at the interface. Overall, this combination of experimental and computational techniques across length scales provides unique insights into the interactions that impact interfacial ion transport and indicates how best to design Li-conducting CPEs with enhanced conductivity. Specifically, tuning the interfacial chemistries and developing methods to quantify the interfacial ion transport pathway is key to CPE design for next-generation Li-ion batteries.

2. Methods

2.1. Density functional theory calculations

Non-spin polarized DFT calculations were done with a plane wave basis set and the projector augmented wave (PAW) method as implemented in the Vienna *Ab Initio* Simulation Package (VASP) 6.3.0.[25–30] The r^{2}SCAN meta-generalized gradient approximation and the r^{2}SCAN + rvv10 meta-generalized gradient approximation (metaGGA) with nonlocal van der Waals corrections were selected as the exchange functional for the bulk and surface calculations, respectively.[31–34] For all the DFT calculations, we utilized the pseudopotentials from the PBE PAW dataset (version 54, September 2015 release). These pseudopotentials, although developed for the Perdew–Burke–Ernzerhof exchange functional, are used for metaGGA calculations as well.[35] Table S1 in the SI provides a list of the specific POTCAR or pseudopotential used for each element in the calculation, which were implemented in our calculations using the MPScanRelaxSet class in pymatgen.[36] An energy convergence criterion between self-consistent cycles of 10^{-5} eV and a force convergence criterion of 0.02 eV Å^{-1} were used in the DFT calculations.

For the bulk LMTO calculations, fully ordered models of the pseudocubic (*P*4/*mmm*) and orthorhombic (*Pnma*) structures were studied. We note that this is not a comprehensive review of the various perovskite polymorphs and configurational complexity, such as partial oxygen occupancy, cation vacancies, and lithium positional disorder and occupancy of interstitial sites, that are possible for the $Li_{0.5-x}M_xLa_{0.5}TiO_3$ (M = Na/K) system.[18] Instead, our bulk LMTO calculations aim to isolate the role of lattice symmetry and A-site chemistry on structural and energetic behavior. Experimental XRD refinement suggests a structure that can be described as cubic or pseudocubic, consistent with the average A-site ionic radii. Accordingly, pseudocubic (*P*4/*mmm*) was selected to represent the high-symmetry limit, while orthorhombic (*Pnma*), which is a common tilted perovskite structure and is a predicted energetically stable $LaTiO_3$ polymorph on the Materials Project database, was used as a representative low-symmetry phase.[16,18,38–53] With this in mind, a structure file of pseudocubic (*P*4/*mmm*) perovskite phase $LaTiO_3$ was obtained from the Inorganic Crystal Structure Database (ICSD) and a structure file of orthorhombic (*Pnma*) perovskite phase $LaTiO_3$ was obtained from the Materials Project database.[18,38–53] Again, the pseudocubic perovskite phase is very nearly cubic, with small TiO_6 octahedral rotations causing a slight distortion in one of the lattice parameters.[18] Both the orthorhombic and pseudocubic crystal structure unit cells along with lattice position descriptions showing the A-site, Ti-site and O-site locations are seen in Fig. S1 in the SI. Special quasirandom structures (SQS) of $Li_{0.5-x}M_xLa_{0.5}TiO_3$ (M = Na or K) were constructed for various *x* compositions ranging from 0 to 0.50 using the integrated cluster expansion toolkit (ICET).[54,55] The SQS supercell sizes were 80 atoms for the pseudocubic structures and 160 atoms for the bulk orthorhombic structures. Full DFT relaxations were then done to allow atom positions and lattice parameters to optimize using the conjugate gradient algorithm.[26] A Monkhorst Pack *k*-point mesh of 8 × 8 × 8 and 6 × 6 × 4 was used for the pseudocubic and orthorhombic unit cells respectively and scaled based on the supercell size of the SQS structures.[56] Decomposition enthalpies (ΔH_d) of the pseudocubic and orthorhombic LMTO structures were calculated using the binary oxides for reference values as:

$$\Delta H_d = E_{Li_{0.5-x}M_xLa_{0.5}TiO_3} - \left[\frac{n_{Li}}{2}E_{Li_2O} + \frac{n_M}{2}E_{M_2O} + \frac{n_{La}}{2}E_{La_2O_3} + n_{Ti}E_{TiO_2}\right], \mathrm{M} = \mathrm{Na} \ \text{ or } \mathrm{K} \qquad (1)$$

where $E_{Li_{0.5-x}M_xLa_{0.5}TiO_3}$ is the DFT computed energy of the LMTO SQS structure, n_i is the number of atoms of species i in the supercell, and $E_{La_2O_3}$, E_{Li_2O}, E_{TiO_2}, and E_{M_2O} are the DFT ground state energy per formula unit of the binary oxides for A-site cations in the LMTO structure.[57] For the binary oxide calculations for reference energies, the same DFT calculation criteria were applied as was done for the bulk LMTO structures.

For the surface DFT calculations, fully ordered LMTO surface models were generated from the cubic perovskite lattice, which provides high-symmetry reference planes and consistent slab construction. During DFT relaxation, LMTO surface atoms are free to distort, effectively capturing local pseudocubic relaxations while avoiding artifacts from pre-imposed low-symmetry distortions. Also, due to the computational cost of these surface calculations, starting from the higher symmetry cubic ($Pm\bar{3}m$) can improve DFT convergence issues and the cubic/pseudocubic distinction is so subtle that surface properties from DFT will not be strongly affected. 4 × 4 supercell (in-plane), symmetric, Ti-terminated LMTO slabs that were 11.877 Å thick, with two AO layers and three TiO_2 layers, composed of 288 atoms, and separated by a vacuum layer approximately 15 Å thick along the orthogonal, (100) direction were generated from the cubic $LaTiO_3$ unit cell.[18,58] Lanthanum atoms were then randomly replaced with lithium, sodium, and potassium atoms to achieve the desired $Li_{0.5-x}M_xLa_{0.5}TiO_3$ composition (*x*), with *x* varying from 0 to 0.5, while still maintaining symmetry within the slab along the orthogonal direction. The A-site composition was also kept constant among all the A-site layers within the slab. Similar to that done for the bulk LMTO DFT models discussed above, compositional complexity, such as partial occupancy of lattice sites and off-center lithium sites that has been reported in LLTO structures, are not considered in our surface LMTO DFT models.[18] This allows us to draw clear conclusions regarding the effect of A-site chemistry with the substitution of Na and K on the A-site lattice on subsequent surface properties.

As previously discussed, in DFT calculations because of the size limitations, the polymer phase is approximated as a polymer fragment or monomer. In our work, the polymer of importance is p(MTFSILi), a Li-conducting and single-ion

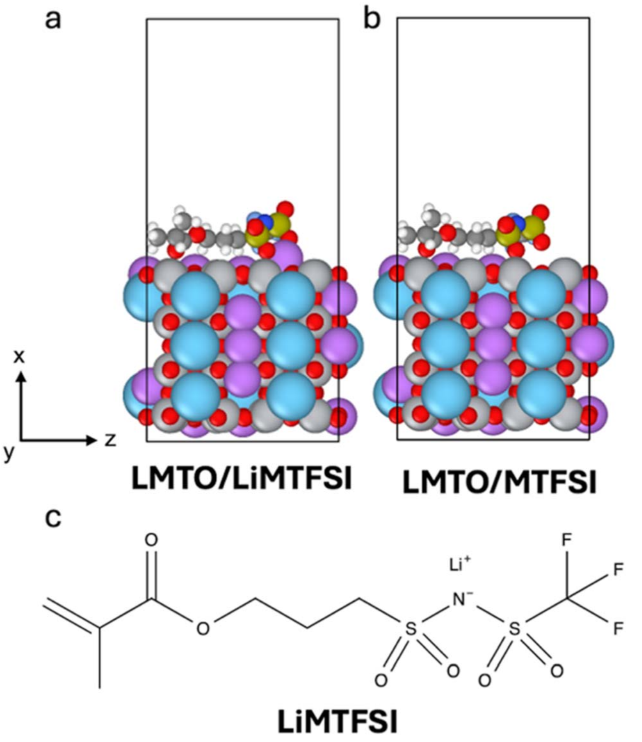

Fig. 2 Example structure of polymer fragment ((a) LiMTFSI and (b) MTFSI) and LMTO slab interface used in DFT surface calculations. (c) Skeletal representation of LiMTFSI polymer fragment.[37]

conducting polymer where the only mobile species in the bulk polymer phase and along the interface is the Li^+ cation. Our work has focused on SIC-based composites since these composites have minimized space charge layers along the polymer-ceramic interface and likely have less tight coordination with Li + cations which is a common issue with dual-ion conducting PEO-based composite electrolytes. Following this, a LiMTFSI polymer fragment structure, with the chemical bonding seen in Fig. 2c, was built using the Amsterdam Modeling Suite with atom positions pre-optimized with the Universal Force Field (UFF).[59,60]

For the following surface and polymer fragment DFT calculations, the atom positions were allowed to fully relax using the conjugate gradient method while the cell volume and shape was held constant. Dipole corrections were also applied along the orthogonal, (100) direction and a Monkhorst Pack *k*-point mesh of 1 × 2 × 2 was used.[56] The atom positions in the middle three layers within the LMTO ceramic slab were held constant during all the calculations using selective dynamics to allow the atoms in the outer layers to relax to their surface-like positions. Three sequential calculations were done for each LMTO slab composition. First, a DFT calculation of the LMTO slab was done. The LiMTFSI polymer fragment was then added as an absorbate approximately 3 Å from the LMTO slab, as seen in Fig. 2a, and a DFT calculation was conducted. The LiMTFSI polymer fragment was placed at the same location across all calculations with the S=O and C=O groups closest to the ceramic slab, following the previous findings with LiTFSI.[15] Finally, the lithium atom from the LiMTFSI was removed, as seen in Fig. 2b, and another DFT relaxation was done. It is important to note that these two subsequent and dependent calculations of LiMTFSI/LMTO then MTFSI/LMTO are required to calculate Li binding energies from eqn (6) and capture the possible interfacial electrostatic interactions in the system. Calculations allowing the atom positions to relax were also done for LiMTFSI and MTFSI polymer fragments in vacuum without the LMTO slab.

From the LMTO slab DFT calculations, the surface energy (γ) of the slabs was calculated as:

$$\gamma = \frac{1}{2A}\left[E_{\mathrm{slab}} - \sum_{\mathrm{i}} n_{\mathrm{i}}\mu_{\mathrm{i}}\right] \tag{2}$$

$$\gamma = \frac{1}{4A}\left[2E_{\mathrm{slab}} - n_{\mathrm{La}}E_{\mathrm{La_2O_3}} - n_{\mathrm{Li}}E_{\mathrm{Li_2O}} - n_{\mathrm{M}}E_{\mathrm{M_2O}} - 2n_{\mathrm{Ti}}E_{\mathrm{TiO_2}}\right], \mathrm{M} = \mathrm{Na}\ \ \mathrm{or\ K} \tag{3}$$

where A is the surface area of one side of the slab, E_{slab} is the DFT calculated energy of the slab, n_{i} is the number of atoms of species i in the slab, μ_{i} is the chemical potential of species i. Note that the binary oxide reference values for the surface energy calculations were bulk DFT calculations with the same criteria as the calculations used for the bulk LMTO calculations but with the r^2SCAN + rvv10 exchange functional since the inclusion of van der Waals interactions shifts the total energy.[31–34]

For the calculations with LiMTFSI and MTFSI adsorbed to the LMTO slab, the adsorption energy and lithium binding energy was calculated with the following equations:

$$E_{\mathrm{ads}}(\mathrm{LiMTFSI}) = E_{\mathrm{DFT}}(\mathrm{LMTO + LiMTFSI}) - E_{\mathrm{DFT}}(\mathrm{LMTO}) - E_{\mathrm{DFT}}(\mathrm{LiMTFSI}) \tag{4}$$

$$E_{\mathrm{ads}}(\mathrm{MTFSI}) = E_{\mathrm{DFT}}(\mathrm{LMTO + MTFSI}) - E_{\mathrm{DFT}}(\mathrm{LMTO}) - E_{\mathrm{DFT}}(\mathrm{MTFSI}) \tag{5}$$

$$E_{\mathrm{bind}}^{\mathrm{Li}} = E_{\mathrm{DFT}}(\mathrm{LMTO + LiMTFSI}) - E_{\mathrm{DFT}}(\mathrm{LMTO + MTFSI}) - E(\mathrm{Li}) \tag{6}$$

where E_{ads}(LiMTFSI) is the adsorption energy of LiMTFSI, E_{ads}(MTFSI) is the adsorption energy of MTFSI to LMTO, and E_{DFT}(i) is the DFT energy of a system with components i, $E_{\mathrm{bind}}^{\mathrm{Li}}$ is the lithium binding energy at the interface, and E(Li) is a lithium reference energy from a bulk lithium metal DFT calculation with the same criteria as the binary oxide references in eqn (3).[15]

$$E_{\mathrm{bind}}^{\mathrm{Li}}(\mathrm{ref}) = E_{\mathrm{DFT}}(\mathrm{LiMTFSI}) - E_{\mathrm{DFT}}(\mathrm{MTFSI}) - E(\mathrm{Li}) \tag{7}$$

A reference lithium binding energy ($E_{\mathrm{bind}}^{\mathrm{Li}}$(ref)) was also calculated from the DFT calculations of just MTFSI and LiMTFSI polymer fragments in vacuum with eqn (7).

For the interfacial DFT structures of LiMTFSI adsorbed to $Li_{0.5}La_{0.5}TiO_3$ (or $Li_{24}La_{24}Ti_{64}O_{176}$), $Li_{0.125}Na_{0.375}La_{0.5}TiO_3$ (or $Li_6Na_{18}La_{24}Ti_{64}O_{176}$), and $Li_{0.125}K_{0.375}La_{0.5}TiO_3$ (or $Li_6K_{18}La_{24}Ti_{64}O_{176}$) LMTO slabs, the electron charge density was written from the converged calculations. Electron charge density difference plots were generated using these written files from these interfacial calculations with VESTA, with the electron charge density difference ($\Delta\rho$) calculated as:

$$\Delta\rho = \rho_{\mathrm{LiMTFSI/Li_6M_{18}La_{24}Ti_{64}O_{176}}} - \rho_{\mathrm{LiMTFSI/Li_{24}La_{24}Ti_{64}O_{176}}}, \\ (\mathrm{M} = \mathrm{Na\ or\ K}) \tag{8}$$

where ρ_i is the electron charge density from the DFT calculation of system composed of i. For the electron charge density difference plots, the electron charge density accumulation and depletion isosurfaces are projected on top of the LiMTFSI/$Li_6M_{18}La_{24}Ti_{64}O_{176}$ structures.

2.2. Flux synthesis of LMTO nanorods

The reaction mixture was prepared by combining P25–TiO_2, $LiNO_3$, $La(NO_3)_3\cdot 6H_2O$, KCl, and NaCl in a mass ratio of 1 : 2 : 0.3 : 2.8 : 2.2. The components were thoroughly ground in an agate mortar and subsequently ball-milled for 5 minutes using a ZrO_2 milling jar. The resulting mixture was dried at 200 °C for 2 hours in a conventional oven, then transferred to an alumina crucible and heated to 800 °C for LMTO-800 nanorods and 900 °C for LMTO-900 nanorods at a rate of 5 K min^{-1} under ambient air for 5 hours to complete the flux reaction. After natural cooling to room temperature, the residual salts were removed by water washing through vacuum filtration. The resulting white solid was dried at 100 °C for 2 hours in a vacuum oven, manually ground into a fine powder, and further calcined at 600 °C for 2 hours in air at a heating rate of 5 °C min^{-1} to yield LMTO-800 and LMTO-900 nanorods.

From our previous work using inductively coupled plasma optical emission spectroscopy (ICP) analysis, the compositions of the LMTO-800 and LMTO-900 nanorods was determined to be $Li_{0.11}Na_{0.243}K_{0.02}La_{0.431}TiO_{2.82}$ and $Li_{0.01}Na_{0.27}K_{0.01}La_{0.51}TiO_{2.71}$, respectively.[16]

2.3. High angle annular dark field STEM and EELS

Samples for the STEM/EELS study were prepared by embedding the nanowires in vacuum-compatible epoxy resin and sectioning the resulting composite with ultramicrotome to be able to observe the nanowires down the long axis. STEM and EELS analysis was carried out using Oak Ridge National Laboratory's (ORNL's) Nion UltraSTEM 200 microscope operated at 200 kV and equipped with Gatan Enfinium EELS spectrometer.

3. Results and discussion

3.1. Phase stability and structure of bulk LMTO

First, we examined the bulk properties and phase stability of $Li_{0.5-x}M_xLa_{0.5}TiO_3$ (M = Na or K) with DFT calculations. To investigate thermodynamic stability, the decomposition enthalpy was calculated for both the LMTO orthorhombic (*Pnma*) and pseudocubic (or tetragonally-distorted cubic) (*P*4/*mmm*) phase, as seen in Fig. 3a. In DFT, decomposition enthalpy is used to show the relative stability of a material compared to a mixture of the most stable corresponding binary oxides, with a more negative decomposition enthalpy indicating the compound is more stable than its binary constituents.[57] It is also used to construct phase diagrams, with differences in decomposition enthalpies showing which phase is more stable.[57] These decomposition enthalpies are calculated at absolute zero and entropic contributions to the thermodynamic stability, which play a big part in cubic and pseudocubic thermodynamic stability especially at higher temperatures, are not represented. Because of the addition of additional cations (Na^+ and K^+) on the A-site lattice, configurational entropy would help to stabilize the higher symmetry cubic or pseudocubic phase.[16] Previous work has shown that r^2SCAN does well, especially compared to other exchange functionals, at predicting decomposition enthalpies.[61] For $Li_{0.5}La_{0.5}TiO_3$ (*i.e.* No Na/K, $x = 0.0$), there is a gap in the decomposition enthalpies of the orthorhombic and pseudocubic phase of approximately 0.045 eV/formula unit, indicating the orthorhombic phase is more thermodynamically stable compared to the pseudocubic phase. As the sodium and potassium composition increases, the decomposition enthalpy gap between the orthorhombic and pseudocubic phases decreases and eventually goes to zero, showing that sodium and potassium help to thermodynamically stabilize the pseudocubic phase. Also from the decomposition enthalpy calculations, we note that potassium plays a larger role in stabilizing the pseudocubic perovskite phase, with the gap in decomposition enthalpies diminishing more rapidly as the potassium, composition increases compared to calculations with sodium. The decomposition enthalpy gap became zero at a Na content around 0.50 and a K content of roughly 0.25. This is consistent with previously reported tolerance factors, where the perovskite polymorph phase stability is predicted based on the ionic radii of the components and when comparing the Shannon ionic radii of potassium, sodium, and lithium which are 1.64 Å, 1.39 Å, and 0.92 Å, respectively, under XII coordination for sodium and potassium and VIII coordination for lithium, since the Shannon ionic radii of lithium is not available at XII coordination.[16,62]

Ionic radii play an important part in perovskite phase stability because if the cation is too small to occupy the large A-site, the TiO_6 will rotate to accommodate the reduced cation size.[16] This can ultimately reduce the long-range Li-ion transport pathways and the symmetry of the crystal structure in the bulk.[63] The main difference separating the orthorhombic, pseudocubic, layered tetragonal, and cubic phases is the degree of TiO_6 rotations and the distribution of A-site cations and vacancies in the lattice.[18] Because of this, the average TiO_6 octahedral rotation angles were obtained by calculating the apical O–O–O bond angle from the bulk LMTO DFT calculations. As seen in Fig. 3b, the average octahedral rotation angle generally decreases with increasing sodium and potassium content, showing an increase in symmetry and stabilization of the pseudocubic phase. Specifically, the average TiO_6 octahedral rotation angles decreases from 10.40° for $x = 0$ ($Li_{0.5}La_{0.5}TiO_3$) to 8.69° for $x = 0.5$ and M = Na ($Na_{0.5}La_{0.5}TiO_3$) and 3.47° for $x = 0.5$, M = K ($K_{0.5}La_{0.5}TiO_3$). This trend in octahedral rotation angles in bulk pseudocubic LMTO ultimately agrees with the calculated decomposition enthalpies. Also agreeing

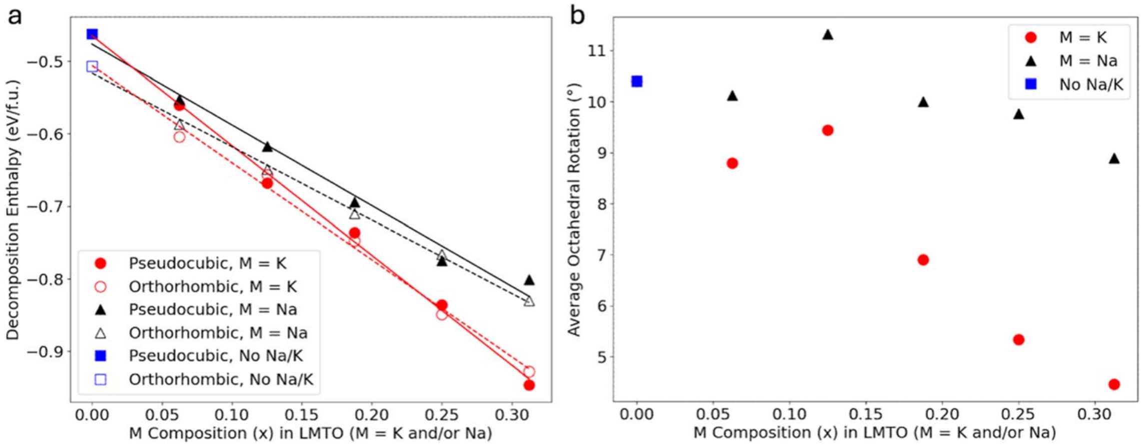

Fig. 3 DFT calculated (a) decomposition enthalpies (ΔH_d) of $Li_{0.5-x}M_xLa_{0.5}TiO_3$ (M = Na or K) for the pseudocubic and orthorhombic phases and (b) average TiO_6 octahedral rotation angles with standard deviation error bars from bulk pseudocubic DFT calculations for $Li_{0.5-x}M_xLa_{0.5}TiO_3$ (M = Na or K).

well with the calculated decomposition enthalpies, the average TiO_6 rotation decreases more with potassium substitution on the A-site lattice compared to sodium substitution. While, in this work, we are focused on inactive LMTO ceramics and not worried about lithium transport within the bulk ceramic, the phase, symmetry, and cation distribution within the lattice plays an important part in the interactions between the polymer and ceramic surface in the CPE. Also, ultimate application of CPEs in next generation energy storage devices, active fillers are essential, so the ability to synthesize the cubic or pseudocubic perovskite LMTO phase with A-site vacancies will be crucial.[7,10] Overall, these bulk calculations show the importance of sodium and potassium at increasing the thermodynamic stability of the pseudocubic LMTO phase compared to the lower symmetry orthorhombic LMTO phase.

From the bulk LMTO calculations of the pseudocubic perovskite phase, the bond length distributions and averages for Li–O, Na–O, K–O, Ti–O, and La–O were extracted. In a perfectly symmetric cubic perovskite $LaTiO_3$ structure, the bond length of all La–O and Ti–O bonds are approximately 2.80 Å and 1.98 Å, with the lanthanum atoms having a coordination number of XII and the titanium atoms having a coordination number of VI. The bonding distribution can tell us more about the symmetry of the structure, with a narrowing of the bond length distribution profile indicating a more highly ordered structure. The element-specific bond length can indicate the strength of the bonding, which can be tracked as a function of sodium and potassium composition. Specifically, the Li–O bond distribution and length, especially more asymmetry or shorter bonds near the dopants, can indicate possible lithium trapping due to local distortions in the A-site environments.[64] The bonding information from the distributions also allows us to gain insight into the coordination of the cations in the crystal structure. For the bulk pseudocubic $Li_{0.5}La_{0.5}TiO_3$ structure, DFT predicted average bond lengths of 2.29 Å, 2.65 Å, and 1.96 Å for the Li–O, La–O, and Ti–O bonds. Compared to the $LaTiO_3$ structure, the La–O bonds are shorter and stronger in $Li_{0.5}La_{0.5}TiO_3$. When sodium and potassium is substituted for lithium on the A-site lattice, the average bond lengths range between 2.09–2.25 Å for Li–O bonds, 2.79–2.82 Å for K–O bonds, 2.57–2.65 Å for Na–O, 2.60–2.69 Å for La–O bonds, and 1.96–1.97 Å for Ti–O bonds. The average bonds lengths for the bulk LMTO structures are plotted *versus* sodium and potassium composition in Fig. S15 and S16. Compared to the $Li_{0.5}La_{0.5}TiO_3$ bulk structure, there are no significant changes in the average Ti–O and La–O bond lengths for the LMTO bulk structures. Of note, the average bond length of Na–O bonds is approximately the same as the La–O bonds (2.57–2.65 Å for Na–O and 2.60–2.69 Å for La–O), while the K–O bonds are on average approximately 0.20 Å longer than the La–O bonds. This is most likely because the Shannon ionic radii of sodium and lanthanum are approximately the same, being 1.39 Å and 1.36 Å respectively under XII coordination, compared to potassium with a much larger Shannon ionic radius of 1.64 Å.[62] Because of this, there is a more narrow distribution in A–O bond lengths in a sodium-containing $LaTiO_3$-based structure ($Na_{0.5}La_{0.5}TiO_3$), reducing the overall disorder of the material which is important for ion conductivity properties.[65] This narrowing of bond length distributions is shown in our data in the bulk $Na_{0.5}La_{0.5}TiO_3$ bond distribution plots and average bond length plots in the SI (Fig. S14 and S16). A slight decrease in the Li–O average bond length, from 2.29 Å in $Li_{0.5}La_{0.5}TiO_3$ to 2.20 Å in $Li_{0.1875}Na_{0.3125}La_{0.5}TiO_3$ and 2.09 Å in $Li_{0.1875}K_{0.3125}La_{0.5}TiO_3$, is observed with the increasing sodium and potassium A-site substitution. This decrease in average Li–O bond length and wide distribution in Li–O bond lengths in the structures with a large doping composition of sodium and potassium could represent a slight increase in the Li–O bond strength and trapping of lithium in asymmetric coordination with suppressed TiO_6 motion, which could promote more lithium trapping in the crystal structure, which would reduce local lithium mobility. This assertion based on the bonding chemistry in our bulk LMTO calculations with varying Na and K content is supported by the experimental findings of Jimenez *et al.*, who found that lithium conductivity decreased with increased Na content in $Li_{0.5-x}Na_xLa_{0.5}TiO_3$ perovskites.[19]

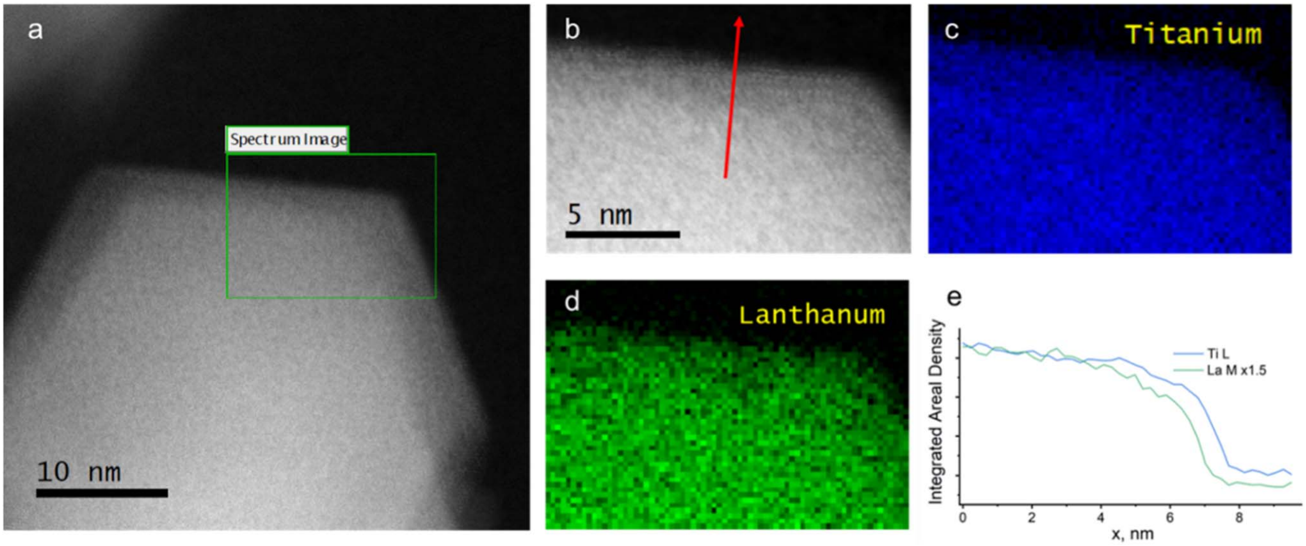

Fig. 4 Faceting and surface chemistry in LMTO-800 nanorods. (a) Overview HAADF STEM image of LMTO nanorod with spectrum image area shown as green box. (b) HAADF STEM image acquired concurrently with Electron Energy Loss (EELS) image over the area in green box; the direction of intensity profile is indicated by a red arrow. (c and d) Areal density maps computed from Ti L and La M edges, respectively. (e) Profiles of the maps in (c and d) taken along the direction indicated in (b) and averaged over ~6.5 nm. Faceting and Ti enrichment/termination at the surface can be clearly seen.

LMTO nanorods reported in our previous work have all acted as inert ceramic fillers, with little to no ionic conductivity.[9,10,16] However, based on our work and knowledge, we know that to achieve significant enhancements in ionic conductivity in CPEs, active ceramics with high ionic conductivities will be necessary.[10] If vacancies were incorporated into the perovskite lattice to use LMTO as active ceramic fillers for CPEs, this decreased Li–O bond length and increase in Li–O bond distribution with sodium and potassium doping could lead to decreased Li-ion conductivity in the bulk ceramic. Further molecular dynamics simulations beyond the scope of this work would be needed to definitively show the impact of Na and K doping on the perovskite A-site lattice's impact on bulk ionic conductivity of the LMTO ceramic with A-site vacancies networks. Therefore, although Na and K helped to stabilize the pseudocubic structure which is favored for higher bulk Li-ion conductivity and seen in experimental XRD data of LMTO nanorods, they also likely trap Li movement by suppressing octahedral flexibility, leading to decreased local ion mobilities in the LMTO ceramic.

3.2. LMTO surface termination

To determine preferential faceting and surface termination of the nanorods, we employed HAADF STEM and EELS mapping. EELS in an aberration-corrected electron microscope is generally capable of identifying chemical identity of a single atomic layer in projection (see *e.g.* Ref. 60 and 61), which would include surface termination and surface element enrichment.[66,67] Two types of LMTO nanorods were examined, LMTO-800 and LMTO-900. The number 800 and 900 refer to the nanorod's flux synthesis temperature (800 and 900 °C, respectively). It was important to find the rods or fragments of rods oriented as close as possible to vertical orientation (along the beam direction), however tilting the sample was problematic due to quickly accumulating beam damage when a convergent probe was stationary on the sample (illumination conditions for tilting). We therefore had to rely on finding the nanorods already in the correct orientation or close to it. Fig. 4a shows an LMTO-800 nanorod in close-to-perpendicular orientation showing (110) pseudocubic facets (orientation determined *via* diffractogram of the image). A region of the top facet (Fig. 4b) was examined with EEL spectrum imaging; Ti and La areal density maps are given in Fig. 4c and d. A profile of both maps taken normal to the top facet and averaged over ~6.5 nm (Fig. 4e) shows that La signal falls off 0.25–0.3 nm before the Ti signal, indicating Ti enrichment at the surface.

LMTO-900 nanorods show consistent behavior with respect to surface chemistry (Fig. 5). In this case we were able to find a nanorod oriented precisely vertical along the beam direction, enabling us to observe high resolution structural information in addition to chemical information. In the case of this nanowire, (110) facets were interspersed with small (100) pseudocubic facets giving overall a rounder shape in cross-section, probably due to smaller overall cross-section of this rod. The region of the EELS spectrum image is marked with a green box on the overview image (Fig. 5a); cubic lattice of the nanorod is well resolved. Some waviness is visible in the HAADF image taken simultaneously with the EELS spectra (Fig. 5b) due to small specimen drift exacerbated by longer dwell times required for EELS spectra collection. The spectral profiles (Fig. 5e) taken along the red arrow direction in Fig. 5b show clear atomic column bumps, with La and Ti out of phase with each other as expected. Ti profile clearly shows extra bumps and enhanced intensity at the surface compared to the La profile. From this dataset it is evident that the nanorod surface is Ti terminated.

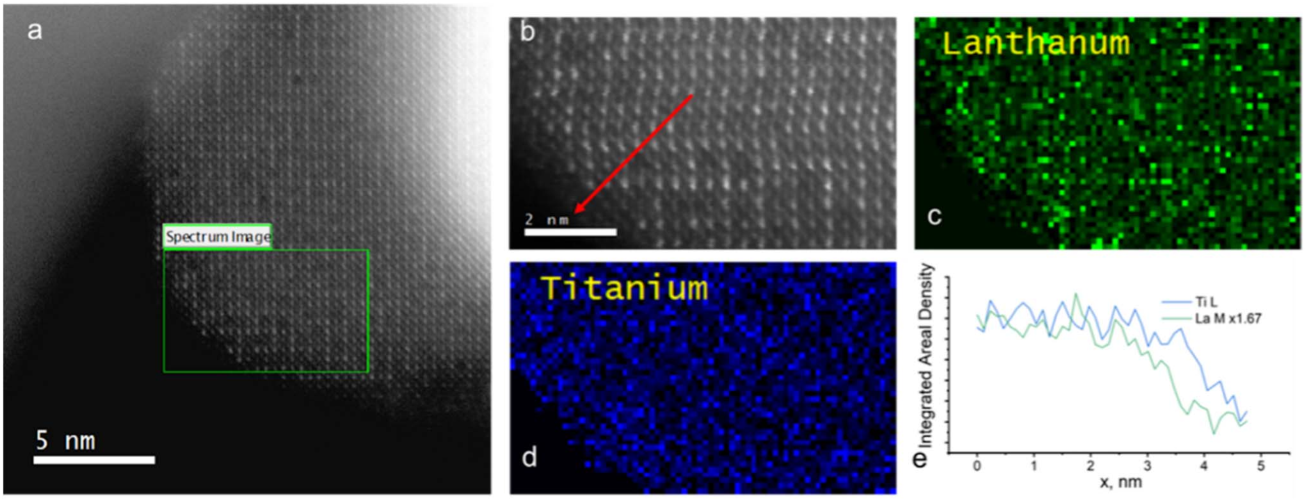

Fig. 5 Faceting and surface chemistry in LMTO-900 nanorods. (a) Overview HAADF STEM image of LMTO-900 nanorod oriented down the long axis with spectrum image area shown as green box. (b) HAADF STEM image acquired concurrently with EELS image over the area in green box; the direction of intensity profile is indicated by a red arrow. (c and d) Areal density maps computed from Ti L and La M edges, respectively. (e) Profiles of the maps in (c and d) taken along the direction indicated in (b) and averaged over ~1.7 nm. Faceting and Ti enrichment/termination at the surface can be clearly seen. Maxima on the elemental profiles correspond to the successive atomic planes.

As reported in our previous work through X-ray diffraction (XRD) characterization of LMTO-800, there are small amounts of Ti-containing impurities, specifically TiO_2 (8.1%) and $La_2Ti_2O_7$ (9.0%), in the LMTO nanorods after the flux synthesis.[16] When the synthesis temperature was increased to 900 °C to produce LMTO-900 nanorods, the $La_2Ti_2O_7$ impurity was eliminated and XRD analysis indicated TiO_2 (9.6%) impurity.[16] From the HAADF-STEM and EELS analysis presented above, the Ti-enrichment of the LMTO nanorod surface was found for the LMTO-800 and LMTO-900 nanorods, showing that the Ti-enrichment of the surface is not attributed to the $La_2Ti_2O_7$ impurity. Additionally, since we observe a continuous lattice in the STEM imaging and do not observe pockets of isolated Ti-rich particles across the surface, as would be expected for segregated TiO_2 phases, we conclude that this Ti-enrichment of the LMTO surface is unlikely to be attributed to the TiO_2 impurity. While inherent heterogeneity along the surface cannot be fully discounted, this STEM and EELS data probing LMTO-800 and LMTO-900 surfaces are consistent in showing a (110)-oriented and Ti-enriched LMTO surface across Na and K compositions and synthesis temperatures.

3.3. Surface stability and structure of LMTO

Following the insights gained from the STEM imaging of the LMTO nanorod surface structure and elemental composition, DFT calculations of Ti-terminated (100)-oriented LMTO ceramic slabs with varying sodium and potassium compositions were done. Although STEM imaging showed that the LMTO-800 and LMTO-900 nanorod surfaces are mostly (110)-oriented, we used the Ti-terminated (100) surface for the DFT calculations because it is a lower index surface that is easier for DFT modeling and convergence while still allowing us to systematically observe the impact of surface chemistry and composition in LMTO that is applicable to the real system. Both the (110) and (100) Ti-enriched surfaces share a Ti–O framework that governs Li coordination at the interface, allowing our model to capture the essential chemistry crucial to surface properties, especially Li and polymer interactions with the surface. From the LMTO ceramic slab only calculations, similar to the bulk LMTO calculations, the average bond lengths, bond length distributions, and average octahedral rotation angles were extracted to compare to the bulk LMTO DFT calculations. For the surface $Li_{0.5}La_{0.5}TiO_3$ calculation, the average bond lengths of Li–O, La–O, and Ti–O was 2.07 Å, 2.73 Å, and 1.96 Å. Compared to the bulk $Li_{0.5}La_{0.5}TiO_3$ average bond lengths reported in Section 3.1, the Li–O average bond length at the surface is approximately 0.22 Å shorter, suggesting that the lithium is more strongly bound to the oxygen atoms at the surface compared to the bulk, and the La–O average bond length at the surface is approximately 0.08 Å longer, suggesting that the lanthanum atoms are slightly less strongly bound to the oxygen at the surface. There is no change in the Ti–O average bond length for $Li_{0.5}La_{0.5}TiO_3$ at the surface compared to the bulk. For the LMTO surface calculations, the average bond lengths of the Li–O, Na–O, K–O, La–O, and Ti–O bonds are approximately 2.03–2.12 Å, 2.69–2.78 Å, 2.82–2.83 Å, 2.73–2.74 Å, and 1.96–1.97 Å. As seen in Fig. S32 and S33, the average Li–O, Na–O, K–O, La–O, and Ti–O bond lengths do not significantly change as the composition of sodium and potassium increases in the LMTO slab. Enhanced Li–O bond strength at the surface, which is indicated by the shorter average Li–O bond lengths at the surface compared to bulk, may promote lithium trapping and decrease surface mobility, potentially accounting for the absence of Li-ion transport from the bulk polymer to the bulk ceramic in prior tracer-exchange NMR studies of LMTO-based composites. When the lithium is more strongly bound to the oxygen at the ceramic surface, the mobility of the lithium atoms at the surface will go down; sodium and potassium ions also likely block Li-ion transport pathways in the crystal structure both at the bulk and at the surface. Similarly to what was seen in the bulk LMTO calculations, the La–O and Na–O average bond lengths are roughly the same at the surface. Bond length distributions were also tracked but no significant changes in distributions were observed as the composition of sodium and potassium was varied; these distributions are reported in the SI for this work.

The average TiO_6 octahedral rotation angle was also calculated from the LMTO slab calculations, and these are reported in Fig. S34 in the SI. In the LMTO slab calculations, we use selective dynamics to fix the atom positions in the middle layers, as seen in the structure in Fig. S34; this allows the atoms in the outer layers to relax to a surface-like configuration. Because of this, the average TiO_6 octahedral rotation angles in the surface calculations are skewed higher by approximately 4–8° compared to the bulk LMTO calculations. Across all of the LMTO slabs modeled, the average TiO_6 octahedral rotation angle is not zero, assuring that pseudocubic distortions are still captured in the surface atoms that were not fixed with selective dynamics after DFT relaxation despite the starting lattice positions being cubic ($Pm\bar{3}m$). As shown in Fig. S34, it is clear that the same trend as calculated for the bulk LMTO models is evident for the surface LMTO models in that the average TiO_6 octahedral rotation angle at the surface decreases with increasing LMTO sodium and potassium composition. When no Li is present in the LMTO DFT slab model ($x = 0.5$), the TiO_6 octahedral tilting is close to zero, specifically 0.41° for M = Na and 0.47° for M = K; this is compared to the TiO_6 octahedral tilting of 2.05° when no Na or K is present in the LMTO slab ($x = 0$). Therefore, even at the surface, the substitution of lithium for larger sodium and potassium cations onto the perovskite A-site lattice helps to increase the symmetry at the surface by reducing the TiO_6 octahedral rotations to a more cubic or pseudocubic-like state. This increased symmetry at the surface can aid in more favorable and continuous electrostatic interactions between the polymer and ceramic phases, which is important for CPE design.

Surface energy calculations from the relaxed DFT LMTO slabs unveil the role that sodium and potassium doping in the perovskite A-site lattice on the (100)-oriented, Ti-terminated surface stability. We report the surface energy results in Fig. S35, where the surface energy is shown to steadily decrease with increasing sodium and potassium content. This shows that doping of sodium and potassium increases the thermodynamic stability of the Ti-terminated (100) surface for the LMTO nanorods, meaning less energy is required to form the surface. To connect to the STEM and EELS analysis presented in Section 3.2, these calculated surface energies indicate that Ti-enrichment of the nanorod LMTO surface is physically reasonable without doing a direct comparison of different surface terminations in DFT. More stable surfaces with lower surface energies are less prone to dissolution and degradation, which can be beneficial for electrolyte applications. This can also indicate that the increased sodium and potassium ion size helps to fulfill the coordination needs of the surface atoms and redistribute the charge density in a more stable configuration. Overall, this thermodynamic surface stability with increasing sodium and potassium doping in the perovskite A-site lattice can be beneficial for CPE applications, specifically for inert ceramic fillers where bulk conductivity in the ceramic is not important for the overall conductivity of the CPE. For active ceramic fillers, a less stable surface (*i.e.* a higher surface energy) can possibly be more reactive with faster Li-ion transport at the interface. It is important for us to reiterate here that one of the goals of this paper is to use static DFT calculations to understand the impact that the A-site LMTO composition has on the LMTO structure, which can correlate to kinetic properties in the CPE, but our DFT outputs are not inherently kinetic properties.

3.4. LMTO interactions with LiMTFSI

Next, because we are ultimately interested in SIC p(MTFSILi)-based CPE applications and interactions between the polymer and the ceramic are important in CPEs, we added a LiMTFSI polymer fragment to the LMTO ceramic slabs and calculated adsorption energies and lithium binding energies, which are presented in Fig. 6a and b. Our work has specifically focused on SIC-based composites since these composites have minimized space charge layers along the polymer-ceramic interface and likely have less tight coordination with Li^+ cations which is a common issue with dual-ion conducting PEO-based composite electrolytes, where both the Li^+ cation and anion are mobile within the polymer matrix. Adsorption energy is a measure of the energy required to separate the polymer fragment from the LMTO slab, representing the strength of the electrostatic interactions between the two components. A negative adsorption energy means that the adsorption process is thermodynamically favored and the adsorbed state, or interface, is lower in energy than if the two components were infinitely separated. Subsequently, an increase in adsorption energy (*i.e.* a less negative adsorption energy) signifies that the adsorption process is less thermodynamically stable and the electrostatic interactions between the polymer fragment and the LMTO slab decreased. Quantifying adsorption energy of the polymer fragment to the ceramic surface is important because electronegative atoms along the polymer chain are known to anchor to the ceramic surface and this anchoring is correlated with interfacial free volume and chain disorder, which has been correlated to interfacial ion transport.[7,68] Additionally, because lithium adsorption at the interface occurs primarily through coordination with surface oxygen atoms, the Ti-enriched surface, as indicated through EELS analysis in Section 3.2, may indirectly influence adsorption energy and Li binding by modifying the local oxygen environment rather than through direct Li^+–Ti^{4+} electrostatic interactions. Therefore, we want to quantify the impact of A-site chemistry in TiO-terminated LMTO slabs on important adsorption and Li binding interactions which can impact the LMTO nanorod performance in composite electrolytes.

The MTFSI adsorption energy for the $Li_{0.5}La_{0.5}TiO_3$ slab with no sodium or potassium doping was calculated to be −3.51 eV. For the slabs with sodium and potassium compositions (x) in $Li_{0.5-x}M_xLa_{0.5}TiO_3$ (M = Na or K), the MTFSI adsorption energy, plotted in Fig. 6a, was shown to steadily decrease, becoming more negative and reaching a minimum of approximately

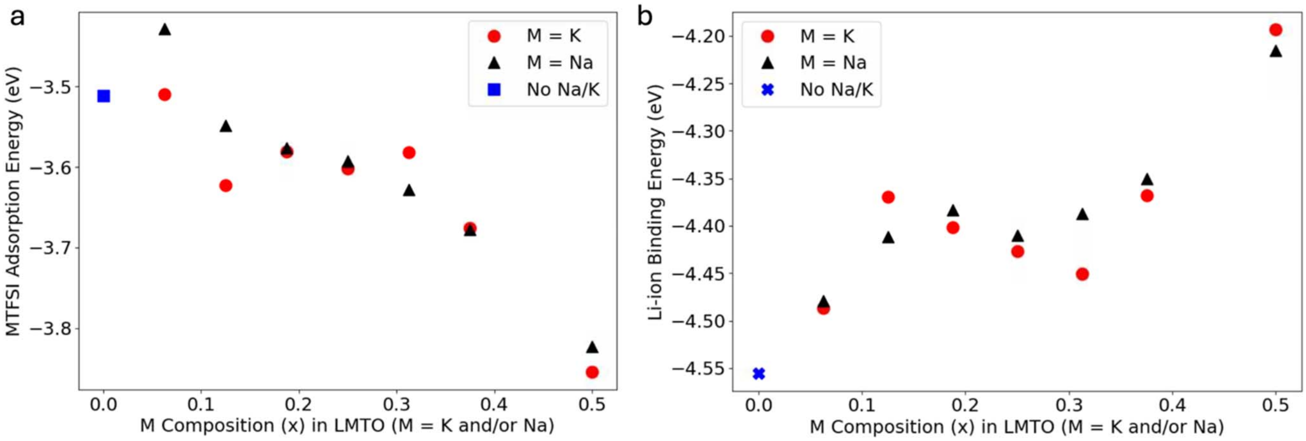

Fig. 6 Calculated (a) MTFSI adsorption energies (E_{ads}(MTFSI)), and (b) lithium binding energy ($E^{\text{Li}}_{\text{bind}}$) from DFT calculations with $\text{Li}_{0.5-x}\text{M}_x\text{La}_{0.5}\text{TiO}_3$ (M = Na or K) ceramic slabs with various M A-site compositions (x).

−3.85 eV. Overall, this signifies that the interface between LMTO and MTFSI becomes more compatible, or thermodynamically favorable, with an increase in the sodium and potassium composition in the LMTO slab. This adsorption energy of the MTFSI polymer fragment to the LMTO slab seen in Fig. 6a is shown to be inversely correlated to the lithium binding energy seen in Fig. 6b where the lithium binding energy becomes less negative as the sodium and potassium composition increases. These DFT results agree with the trend reported in previous literature, where the stronger the MTFSI is bound, or adsorbed, to the ceramic surface, the higher the Li binding energy, or the less strongly bound the lithium atom is.[15] The lithium binding energy is the strength of the bond between the lithium atom, which is our mobile species in the CPE, and the MTFSI polymer fragment, which is our immobile anion species in the CPE. If the lithium binding energy increases (*i.e.* becomes less negative), this means that the lithium atom is less strongly bound to the MTFSI, or the energy required to dissociate the lithium from the MTFSI, is lower. This is correlated to a more mobile lithium atom and decreased resistance to Li-ion transport along the interface. There is no such correlation observed between the LiMTFSI adsorption energies, plotted in Fig. S36 in the SI, and the MTFSI adsorption energies or lithium binding energies.

When compared to the reference LiMTFSI Li binding energy ($E^{\text{Li}}_{\text{bind}}$(ref)), which was calculated to be −4.35 eV, the Li binding energy when the LiMTFSI is adsorbed to the LMTO slabs with Na and K compositions below $x = 0.5$ is lower, meaning the lithium is more strongly bound to the MTFSI anion at the interface compared to in vacuum, which is used to represent the bulk polymer state. This physically makes sense since the potential energy landscapes are different at the interface compared to in bulk, with the lithium atom being energetically shared by both the polymer and the ceramic surface at the interface and can explain the long-standing observation of interfacial transport resistance in CPEs. As the sodium and potassium substitution for lithium on the A-site perovskite lattice increases, the lithium binding energy generally approaches the reference LiMTFSI Li binding energy and, at $x = 0.5$, the Li binding energy at the interface goes above the reference LiMTFSI Li binding energy, as seen in Fig. 6b, while maintaining strong MTFSI adsorption to LMTO. This indicates that the Li-ion is more mobile at the polymer/$\text{La}_{0.5}\text{M}_{0.5}\text{TiO}_3$ (M = Na or K) interface than in the bulk polymer phase. Overall, this increase in lithium binding energy with increasing Na and K compositions signifies an increase in Li-ion mobility along the polymer-ceramic interface as the composition changes. We would like to reiterate here that for all the DFT calculations, the LiMTFSI polymer fragment was added to the LMTO slab at the same location and then positions were allowed to relax. This means that the differences in Li binding energy and adsorption energy seen across the LMTO slabs are solely due to changes in the electrostatic interactions between the LMTO slab and LiMTFSI polymer fragment. We hypothesize that as the lithium binding energy at the interface approaches the lithium binding energy of the polymer fragment in vacuum, the resistance to lithium transport along the interface goes away, meaning interfacial lithium transport increases thus increasing the ionic conductivity of the CPE. For small cations, such as lithium, electrostatic interactions are known to be the main contributor to ion transport in polymer electrolytes, as shown through the Anderson-Stuart model.[1] Therefore, an increase in favorable electrostatic interactions and increase in lithium mobility at the interface is assumed to be directly correlated to a decrease in the activation barrier for interfacial Li-ion transport and thus an increase in ionic conductivity attributed to interfacial transport.

While the trend of MTFSI adsorption energy and lithium binding energy across LMTO compositions is generally consistent, a small number of data points slightly deviate, notably $x = 0.0625$ (Na), $x = 0.125$ (K), and $x = 0.3125$ (K), as shown in Fig. 6 and S36. These deviations in adsorption and lithium binding energies occur despite maintaining identical LiMTFSI initial orientation and placement across all LMTO slabs and are not due to differences in the slab surface energies, which vary linearly with LMTO composition, as observed in Fig. S35. Slight deviations possibly occur due to the multi-step relaxation of the DFT calculations, where the MTFSI adsorption energy, and thus lithium binding energy, relies on the final relaxed structure from the LiMTFSI adsorption structures, which slightly vary

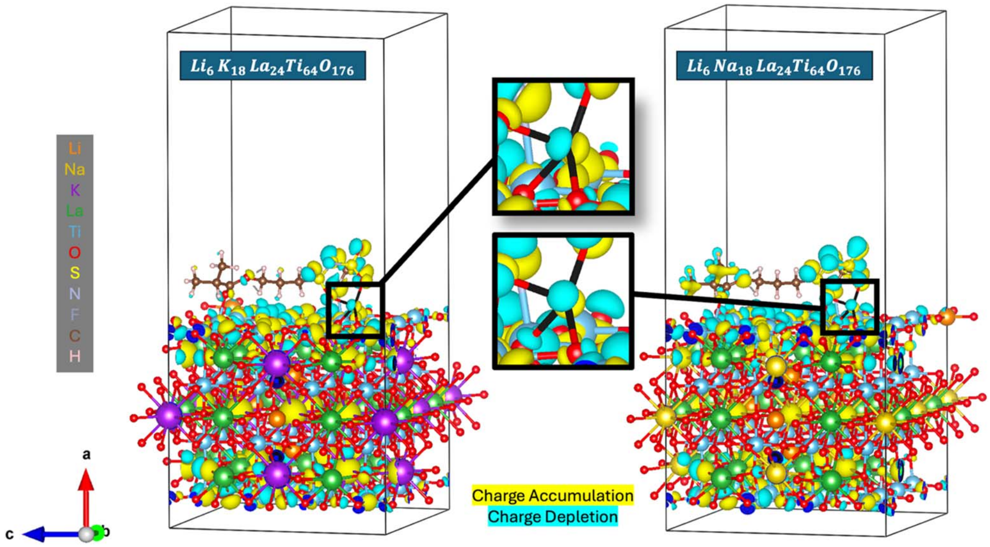

Fig. 7 Electron density difference plots comparing electron density of the (left) LiMTFSI/$Li_6K_{18}La_{24}Ti_{64}O_{176}$ and (right) LiMTFSI/$Li_6Na_{18}La_{24}Ti_{64}O_{176}$ calculated structures with the electron density of the LiMTFSI/$Li_{24}La_{24}Ti_{64}O_{176}$ calculated structure generated with Vesta, with charge accumulation isosurfaces colored yellow and charge depletion isosurfaces colored light blue.[70] The Li coordinated to the MTFSI polymer fragment is removed for clarity of isosurfaces around it, but it's coordination (colored black) is zoomed in on at the center of the figure for both structures.

between LMTO slab composition structures. Because of the large simulation cell size, complex local cation environments from A-site compositional changes, and the computational cost of fully sampling all possible adsorbate and dopant configurations and orientations, we attribute these deviations to a combination of genuine local chemical effects and residual numerical uncertainty inherent in slab–adsorbate DFT calculations. Such variability is typical for large polar adsorbates on mixed-cation oxide surfaces and we believe this does not affect the overall conclusions drawn from the observed compositional trends above in Fig. 6.[69]

In Fig. 7, electron charge density difference plots are shown comparing the charge density of the LMTO/LiMTFSI calculations with the charge density of the LLTO/LiMTFSI calculation. These electron charge density difference plots show where there is electron density accumulation and depletion in the interfacial LMTO/LiMTFSI structures compared to similar LLTO/LiMTFSI interfacial structures without Na and K substituted onto the A-site perovskite lattice. When comparing the charge density around the mobile Li that is coordinated to the MTFSI polymer fragment, there is charge accumulation away from the MTFSI and toward the LMTO slab, as seen in the zoomed in images in Fig. 7. This means that the electron charge density around the mobile Li accumulates more toward the LMTO slab when compared to the LLTO slab (*i.e.* the electron charge density is farther from the MTFSI polymer fragment). This supports the Li binding energy results that suggest that the Li charge is more delocalized from the MTFSI anion at the LMTO interface compared to the LLTO interface due to the addition of Na and K on the A-site lattice, which increases the electrostatic interactions between the MTFSI and LMTO. As shown in Section 3.3, the substitution of Na and K on the A-site lattice changes the bonding character and TiO_6 octahedral tilting at the LMTO surface, which can thus impact the Li electrostatic interactions with the LMTO surface oxygen atoms, which is shown from the Li binding energy calculations and Li charge accumulation near the LMTO interface compared to the LLTO interface in Fig. 7. Therefore, based on our surface calculations of LMTO with varying A-site compositions of Li, Na, and K and a LiMTFSI polymer fragment, we conclude that the replacement of Li for Na and K into the A-site lattice will increase the Li-ion transport along the polymer-ceramic interface in the CPE by increasing the energetic stability of the LMTO and p(MTFSI) interface, further delocalizing the Li^+ charge from the $MTFSI^-$. This assertion from our DFT calculations is supported by our previous experimental work that showed a two-fold increase in ionic conductivity attributed to a percolating interfacial transport network in the LMTO-800 nanorod based composite electrolyte opposed to commercially available LLTO particle based composites and rutile TiO_2 based composites.[9,16]

Our results indicate that the sodium-containing and potassium-containing alternative to A-site disordered pseudo-cubic perovskite $Li_{0.5}La_{0.5}TiO_3$ would be good inert ceramic fillers for p(MTFSILi)-based composite electrolytes. Specifically, p(MTFSILi)-based CPEs with inert LMTO fillers with increased Na and K compositions will have increased Li-ion transport along the interface and thus increased overall ionic conductivity. This suggests that Li content in the inert ceramic filler is not necessary for improved Li-ion interfacial transport in CPE design for solid-state Li-ion batteries, which is significant due to the limited availability and cost of Li resources. Ultimately, in order to achieve significant enhancements in ionic conductivity in composite electrolytes (on the order of 10 to 100 fold enhancements), it has been suggested that superionic ceramics fillers with non-negligible bulk conductivity will be necessary to achieve ion exchange across the polymer-ceramic interface.[10]

This could indicate that, if future work was done to synthesize a highly active LMTO ceramic, adding Na and/or K to the A-site perovskite lattice could negatively impact the bulk LMTO conductivity and thus interfacial Li-ion exchange across the polymer-ceramic interface while simultaneously improving Li-ion transport along the interface, so one would need to balance this tradeoff to design a composite electrolyte with optimal transport both along and across the interface. Also, for future work since LMTO could be used in Na- and K-conducting electrolytes, it would be interesting to extend this work on interfacial Li-ion transport for applications in Li-ion batteries to determine the impact that LMTO A-site composition has on Na and K binding energy and Na-ion and K-ion interfacial transport for applications in sodium–ion and potassium–ion batteries. We do note, however, that sodium lanthanum titanate, the sodium-conducting alternative to LLTO, is generally not considered a good sodium–ion conductor.[19,65]

4. Conclusions

This work uses a combination of DFT calculations and STEM and EELS measurements to reveal the role that the A-site lattice composition in $La_{0.5}Li_{0.5-x}M_xTiO_3$ (M = Na, K) (LMTO) has on the bulk and surface crystal structure and interactions of LMTO with LiMTFSI, which are important for CPE applications in future Li-ion battery technologies. From the bulk LMTO DFT calculations, decomposition enthalpy calculations showed that increased sodium and potassium compositions in LMTO increase the thermodynamic stability of the pseudocubic perovskite phase compared to the lower-symmetry orthorhombic phase. This is attributed to the increased ionic radii of sodium and potassium compared to lithium, which also leads to reduced TiO_6 octahedral rotations indicating a higher symmetry structure and a slightly smaller Li–O bond length. HAADF STEM and EELS measurements were used to unveil the surface elemental composition and facet orientation of the experimentally synthesized LMTO nanorods, using the newly developed flux synthesis method.[16] It was shown that the LMTO nanorods, even when having different A-site lattice compositions due to the synthesis temperature, have a (110)-oriented interspersed with a small amount of (100)-oriented and Ti-enriched surface. Finally, we used surface LMTO DFT calculations to quantify the LiMTFSI and MTFSI adsorption energies, quantifying the strength of the interactions of the polymer, represented as a polymer fragment, with LMTO for various sodium and potassium compositions. These adsorption energies were correlated with the lithium binding energies of Li to MTFSI when adsorbed on the LMTO surface. We showed that increasing the sodium and potassium surface chemistry composition in LMTO can strengthen the compatibility of the polymer (p(LiMTFSI)) and ceramic (LMTO) phases, allowing for the lithium charge to be more delocalized from the MTFSI anion and thus more mobile at the polymer-ceramic interface, ultimately increasing interfacial Li-ion conductivity. Overall, detailed DFT calculations revealed that Na and K doping into LMTO is beneficial for improving the ion transport rate of the polymer phase near the surface of the LMTO nanorods. However, Na and K doping can also simultaneously decrease Li mobility within the LMTO ceramic phase, contributing to increased ion transport resistance and ion exchange times across the polymer-ceramic interface. These results showcase the importance of performing comprehensive, interdisciplinary studies to understand how the bulk structure and surface interactions at the atomic level between the polymer and ceramic phases can impact properties that are crucial for targeted CPE design for next-generation Li-ion batteries.

Author contributions

L. B. Shepard: conceptualization, methodology, investigation, formal analysis, validation, visualization, data curation, writing – original draft, writing – review & editing; A. B. Borisevich: conceptualization, methodology, investigation, formal analysis, validation, visualization, data curation, writing – original draft, writing – review & editing; T. Wang: methodology, investigation, writing – review & editing; J. Ock: conceptualization, writing – review & editing; A. P. Sokolov: conceptualization, supervision, project administration, funding acquisition, writing – review & editing; X. C. Chen: conceptualization, supervision, project administration, funding acquisition, writing – review & editing; S. Dai: supervision, project administration, funding acquisition, writing – review & editing; S. B. Sinnott: conceptualization, supervision, project administration, funding acquisition, writing – review & editing.

Conflicts of interest

The authors declare no conflicts of interest. This manuscript has been authored by UT-Battelle, LLC, under contract DE-AC05-00OR22725 with the U.S. Department of Energy. The United State government retai3/2/2026 3:32:00 pMns and the publisher, by accepting the article for publication, acknowledges that the United States government retains a nonexclusive, paid-up, irrevocable, world-wide license to publish or reproduce the published form of this manuscript or allow others to do so for United States government purposes. The Department of Energy will provide public access to these results of federally sponsored research in accordance with the DOE Public Access Plan (https://www.energy.gov/downloads/doepublic-access-plan).

Data availability

The raw data and codes used for the Density Functional Theory calculations and corresponding data, analysis, and visualization are publicly available on Zenodo.[71] All other data used in this study are available from the corresponding authors upon reasonable request.

Supplementary information (SI): cubic perovskite unit cell graphic (Fig. S1); list of PAW pseudopotentials used in DFT calculations (Table 1); Li–O, La–O, Ti–O, Na–O, and K–O bond length distributions from bulk LMTO DFT calculations (Fig. S2–S14); average Li–O, La–O, Ti–O, and K–O bond lengths from bulk $Li_{0.5-x}K_xLa_{0.5}TiO_3$ calculations (Fig. S15); average Li–O, La–O, Ti–O, and Na–O bond lengths from bulk $Li_{0.5-x}Na_xLa_{0.5}TiO_3$

calculations (Fig. S16); Li–O, La–O, Ti–O, Na–O, and K–O bond length distributions from surface LMTO DFT calculations (Fig. S17–S31); average Li–O, La–O, Ti–O, and K–O bond lengths from surface $Li_{0.5-x}K_xLa_{0.5}TiO_3$ calculations (Fig. S32); average Li–O, La–O, Ti–O, and Na–O bond lengths from surface $Li_{0.5-x}Na_xLa_{0.5}TiO_3$ calculations (Fig. S33); average TiO_6 octahedral rotation angles from surface $Li_{0.5-x}M_xLa_{0.5}TiO_3$ (M = Na, K) calculations (Fig. S34); Calculated LMTO slab surface energies from surface $Li_{0.5-x}M_xLa_{0.5}TiO_3$ (M = Na, K) calculations (Fig. S35); LiMTFSI adsorption energies from surface $Li_{0.5-x}M_xLa_{0.5}TiO_3$ (M = Na, K) calculations (Fig. S36). See DOI: https://doi.org/10.1039/d5ta10111e.

Acknowledgements

This work was supported by the Fast and Cooperative Ion Transport in Polymer Electrolytes (FaCT) Energy Frontier Research Center (EFRC) funded through the U.S. Department of Energy (DOE), Office of Science, Basic Energy Sciences hosted at Oak Ridge National Laboratory (ORNL). The DFT calculations done for this work utilized the Roar Collab high performance research computing cluster managed by the Institute for Computational and Data Sciences at The Pennsylvania State University. The STEM and EELS measurements reported here utilized the resources at the Center for Nanophase Materials Sciences (CNMS), a DOE Office of Science User Facility at ORNL. LB Shepard and SB Sinnott would like to acknowledge Valentino R. Cooper for his assistance in the revisions of this manuscript.

References

1 V. Bocharova and A. P. Sokolov, *Macromolecules*, 2020, **53**, 4141–4157.
2 S. Li, S.-Q. Zhang, L. Shen, Q. Liu, J.-B. Ma, W. Lv, Y.-B. He and Q.-H. Yang, *Adv. Sci.*, 2020, **7**, 1903088.
3 H. Yang and N. Wu, *Energy Sci. Eng.*, 2022, **10**, 1643–1671.
4 Q. Zhu, Y. Liu, L. B. Shepard, D. Bhattacharya, S. B. Sinnott, W. F. Reinhart, V. R. Cooper and R. Kumar, *Chem. Mater.*, 2024, **36**, 11934–11946.
5 K. Daems, P. Yadav, K. B. Dermenci, J. Van Mierlo and M. Berecibar, *Renew. Sustain. Energy Rev.*, 2024, **191**, 114136.
6 Y. Horowitz, M. Lifshitz, A. Greenbaum, Y. Feldman, S. Greenbaum, A. P. Sokolov and D. Golodnitsky, *J. Electrochem. Soc.*, 2020, **167**, 160514.
7 S. C. Sand, J. L. M. Rupp and B. Yildiz, *Chem. Soc. Rev.*, 2025, **54**, 178–200.
8 J. Lu and Y. Li, *J. Mater. Sci. Mater. Electron.*, 2021, **32**, 9736–9754.
9 J. Ock, A. Bhattacharya, T. Wang, C. Gainaru, Y. Wang, K. L. Browning, M. Lehmann, M. A. Rahman, M. Chi, F. Wang, J. K. Keum, L. Kearney, T. Saito, S. Dai, R. J. Clément, A. P. Sokolov and X. C. Chen, *Macromolecules*, 2024, **57**, 7489–7498.
10 A. Bhattacharya, J. Ock, T. Wang, J. T. Bamford, R. A. Segalman, S. Dai, A. P. Sokolov, X. C. Chen and R. J. Clément, *Solid State Ionics*, 2025, **428**, 116938.
11 D. Spencer Jolly, D. L. R. Melvin, I. D. R. Stephens, R. H. Brugge, S. D. Pu, J. Bu, Z. Ning, G. O. Hartley, P. Adamson, P. S. Grant, A. Aguadero and P. G. Bruce, *Inorganics*, 2022, **10**, 60.
12 J. Peng, Y. Xiao, D. A. Clarkson, S. G. Greenbaum, T. A. Zawodzinski and X. C. Chen, *ACS Appl. Polym. Mater.*, 2020, **2**, 1180–1189.
13 X. C. Chen, X. Liu, A. Samuthira Pandian, K. Lou, F. M. Delnick and N. J. Dudney, *ACS Energy Lett.*, 2019, **4**, 1080–1085.
14 C. Gainaru, R. Kumar, I. Popov, M. A. Rahman, M. Lehmann, E. Stacy, V. Bocharova, B. G. Sumpter, T. Saito, K. S. Schweizer and A. P. Sokolov, *Macromolecules*, 2023, **56**, 6051–6059.
15 N. Wu, P.-H. Chien, Y. Qian, Y. Li, H. Xu, N. S. Grundish, B. Xu, H. Jin, Y.-Y. Hu, G. Yu and J. B. Goodenough, *Angew. Chem.*, 2020, **132**, 4160–4166.
16 T. Wang, J. Ock, X. C. Chen, F. Wang, M. Li, M. S. Chambers, G. M. Veith, L. B. Shepard, S. B. Sinnott, A. Borisevich, M. Chi, A. Bhattacharya, R. J. Clément, A. P. Sokolov and S. Dai, *Adv. Sci.*, 2025, **12**, 2408805.
17 A. Várez, J. Ibarra, A. Rivera, C. León, J. Santamaría, M. A. Laguna, M. L. Sanjuán and J. Sanz, *Chem. Mater.*, 2003, **15**, 225–232.
18 M. Sommariva and M. Catti, *Chem. Mater.*, 2006, **18**, 2411–2417.
19 R. Jimenez, A. Rivera, A. Varez and J. Sanz, *Solid State Ionics*, 2009, **180**, 1362–1371.
20 M. Catti, M. Sommariva and R. M. Ibberson, *J. Mater. Chem.*, 2007, **17**, 1300–1307.
21 J. M. S. Skakle, G. C. Mather, M. Morales, R. I. Smith and A. R. West, *J. Mater. Chem.*, 1995, **5**, 1807–1808.
22 M. S. Chambers, J. Chen, R. L. Sacci, R. D. McAuliffe, W. Sun and G. M. Veith, *Chem. Mater.*, 2024, **36**, 1197–1213.
23 M. E. Sotomayor, B. Levenfeld, A. Varez and J. Sanz, *J. Alloys Compd.*, 2017, **720**, 460–465.
24 W. Liu, S. W. Lee, D. Lin, F. Shi, S. Wang, A. D. Sendek and Y. Cui, *Nat. Energy*, 2017, **2**, 17035.
25 G. Kresse and J. Furthmüller, *Comput. Mater. Sci.*, 1996, **6**, 15–50.
26 G. Kresse and J. Furthmüller, *Phys. Rev. B:condens. Matter Mater. Phys.*, 1996, **54**, 11169–11186.
27 G. Kresse and J. Hafner, *J. Phys. Condens. Matter*, 1994, **6**, 8245.
28 G. Kresse and J. Hafner, *Phys. Rev. B:condens. Matter Mater. Phys.*, 1993, **47**, 558–561.
29 G. Kresse and D. Joubert, *Phys. Rev. B:condens. Matter Mater. Phys.*, 1999, **59**, 1758–1775.
30 P. E. Blöchl, *Phys. Rev. B:condens. Matter Mater. Phys.*, 1994, **50**, 17953–17979.
31 J. W. Furness, A. D. Kaplan, J. Ning, J. P. Perdew and J. Sun, *J. Phys. Chem. Lett.*, 2020, **11**, 8208–8215.
32 J. Ning, M. Kothakonda, J. W. Furness, A. D. Kaplan, S. Ehlert, J. G. Brandenburg, J. P. Perdew and J. Sun, *Phys. Rev. B*, 2022, **106**, 075422.
33 J. Klimeš, D. R. Bowler and A. Michaelides, *J. Phys. Condens. Matter*, 2009, **22**, 022201.

34 J. Klimeš, D. R. Bowler and A. Michaelides, *Phys. Rev. B:condens. Matter Mater. Phys.*, 2011, **83**, 195131.
35 R. Kingsbury, A. S. Gupta, C. J. Bartel, J. M. Munro, S. Dwaraknath, M. Horton and K. A. Persson, *Phys. Rev. Mater.*, 2022, **6**, 013801.
36 S. P. Ong, W. D. Richards, A. Jain, G. Hautier, M. Kocher, S. Cholia, D. Gunter, V. L. Chevrier, K. A. Persson and G. Ceder, *Comput. Mater. Sci.*, 2013, **68**, 314–319.
37 A. Stukowski, *Modell. Simul. Mater. Sci. Eng.*, 2009, **18**, 015012.
38 A. Jain, S. P. Ong, G. Hautier, W. Chen, W. D. Richards, S. Dacek, S. Cholia, D. Gunter, D. Skinner, G. Ceder and K. A. Persson, *APL Mater.*, 2013, **1**, 011002.
39 I. Petousis, D. Mrdjenovich, E. Ballouz, M. Liu, D. Winston, W. Chen, T. Graf, T. D. Schladt, K. A. Persson and F. B. Prinz, *Sci. Data*, 2017, **4**, 160134.
40 J. M. Munro, K. Latimer, M. K. Horton, S. Dwaraknath and K. A. Persson, *npj Comput. Mater.*, 2020, **6**, 112.
41 A. K. Singh, L. Zhou, A. Shinde, S. K. Suram, J. H. Montoya, D. Winston, J. M. Gregoire and K. A. Persson, *Chem. Mater.*, 2017, **29**, 10159–10167.
42 A. M. Patel, J. K. Nørskov, K. A. Persson and J. H. Montoya, *Phys. Chem. Chem. Phys.*, 2019, **21**, 25323–25327.
43 K. A. Persson, B. Waldwick, P. Lazic and G. Ceder, *Phys. Rev. B:condens. Matter Mater. Phys.*, 2012, **85**, 235438.
44 M. K. Horton, J. H. Montoya, M. Liu and K. A. Persson, *npj Comput. Mater.*, 2019, **5**, 64.
45 H. Ding, S. S. Dwaraknath, L. Garten, P. Ndione, D. Ginley and K. A. Persson, *ACS Appl. Mater. Interfaces*, 2016, **8**, 13086–13093.
46 A. Jain, G. Hautier, C. J. Moore, S. Ping Ong, C. C. Fischer, T. Mueller, K. A. Persson and G. Ceder, *Comput. Mater. Sci.*, 2011, **50**, 2295–2310.
47 A. Wang, R. Kingsbury, M. McDermott, M. Horton, A. Jain, S. P. Ong, S. Dwaraknath and K. A. Persson, *Sci. Rep.*, 2021, **11**, 15496.
48 M. Aykol, S. S. Dwaraknath, W. Sun and K. A. Persson, *Sci. Adv.*, 2018, **4**, eaaq0148.
49 R. Tran, Z. Xu, B. Radhakrishnan, D. Winston, W. Sun, K. A. Persson and S. P. Ong, *Sci. Data*, 2016, **3**, 160080.
50 M. de Jong, W. Chen, H. Geerlings, M. Asta and K. A. Persson, *Sci. Data*, 2015, **2**, 150053.
51 M. de Jong, W. Chen, T. Angsten, A. Jain, R. Notestine, A. Gamst, M. Sluiter, C. Krishna Ande, S. van der Zwaag, J. J. Plata, C. Toher, S. Curtarolo, G. Ceder, K. A. Persson and M. Asta, *Sci. Data*, 2015, **2**, 150009.
52 K. Latimer, S. Dwaraknath, K. Mathew, D. Winston and K. A. Persson, *npj Comput. Mater.*, 2018, **4**, 40.
53 H. Zheng, X.-G. Li, R. Tran, C. Chen, M. Horton, D. Winston, K. A. Persson and S. P. Ong, *Acta Mater.*, 2020, **186**, 40–49.
54 A. Zunger, S.-H. Wei, L. G. Ferreira and J. E. Bernard, *Phys. Rev. Lett.*, 1990, **65**, 353–356.
55 M. Ångqvist, W. A. Muñoz, J. M. Rahm, E. Fransson, C. Durniak, P. Rozyczko, T. H. Rod and P. Erhart, *Adv. Theory Simul.*, 2019, **2**, 1900015.
56 H. J. Monkhorst and J. D. Pack, *Phys. Rev. B*, 1976, **13**, 5188–5192.
57 C. J. Bartel, A. W. Weimer, S. Lany, C. B. Musgrave and A. M. Holder, *npj Comput. Mater.*, 2019, **5**, 4.
58 A. Hjorth Larsen, J. Jørgen Mortensen, J. Blomqvist, I. E. Castelli, R. Christensen, M. Dułak, J. Friis, M. N. Groves, B. Hammer, C. Hargus, E. D. Hermes, P. C. Jennings, P. Bjerre Jensen, J. Kermode, J. R. Kitchin, E. Leonhard Kolsbjerg, J. Kubal, K. Kaasbjerg, S. Lysgaard, J. Bergmann Maronsson, T. Maxson, T. Olsen, L. Pastewka, A. Peterson, C. Rostgaard, J. Schiøtz, O. Schütt, M. Strange, K. S. Thygesen, T. Vegge, L. Vilhelmsen, M. Walter, Z. Zeng and K. W. Jacobsen, *J. Phys. Condens. Matter*, 2017, **29**, 273002.
59 A. K. Rappe, C. J. Casewit, K. S. Colwell, W. A. Goddard and W. M. Skiff, *J. Am. Chem. Soc.*, 1992, **114**, 10024–10035.
60 E. J. Baerends, N. F. Aguirre, N. D. Austin, J. Autschbach, F. M. Bickelhaupt, R. Bulo, C. Cappelli, A. C. T. Van Duin, F. Egidi, C. Fonseca Guerra, A. Förster, M. Franchini, T. P. M. Goumans, T. Heine, M. Hellström, C. R. Jacob, L. Jensen, M. Krykunov, E. Van Lenthe, A. Michalak, M. M. Mitoraj, J. Neugebauer, V. P. Nicu, P. Philipsen, H. Ramanantoanina, R. Rüger, G. Schreckenbach, M. Stener, M. Swart, J. M. Thijssen, T. Trnka, L. Visscher, A. Yakovlev and S. Van Gisbergen, *J. Chem. Phys.*, 2025, **162**, 162501.
61 M. Kothakonda, A. D. Kaplan, E. B. Isaacs, C. J. Bartel, J. W. Furness, J. Ning, C. Wolverton, J. P. Perdew and J. Sun, *arXiv*, 2022, preprint, arXiv:2208.02841, DOI: 10.48550/arXiv.2208.02841.
62 R. D. Shannon, *Acta Crystallogr., Sect. A*, 1976, **32**, 751–767.
63 J. Wu, L. Chen, T. Song, Z. Zou, J. Gao, W. Zhang and S. Shi, *Funct. Mater. Lett.*, 2017, **10**(3), 1730002.
64 Y. Liang, F. Li, X. Cui, C. Stampfl, S. P. Ringer, X. Yang, J. Huang and R. Zheng, *Sci. Adv.*, 2025, **11**(11), eads7054.
65 A. R. Symington, J. Purton, J. Statham, M. Molinari, M. Saiful Islam and S. C. Parker, *J. Mater. Chem. A*, 2020, **8**, 19603–19611.
66 I. MacLaren and Q. M. Ramasse, *Int. Mater. Rev.*, 2014, **59**, 115–131.
67 M. Varela, J. Gazquez, T. J. Pennycook, C. Magen, M. P. Oxley and S. J. Pennycook, in *Scanning Transmission Electron Microscopy: Imaging and Analysis*, ed. S. J. Pennycook and P. D. Nellist, Springer, New York, NY, 2011, pp. 429–466.
68 F. Croce, L. Persi, B. Scrosati, F. Serraino-Fiory, E. Plichta and M. A. Hendrickson, *Electrochim. Acta*, 2001, **46**, 2457–2461.
69 A. J. R. Hensley, K. Ghale, C. Rieg, T. Dang, E. Anderst, F. Studt, C. T. Campbell, J.-S. McEwen and Y. Xu, *J. Phys. Chem. C*, 2017, **121**, 4937–4945.
70 K. Momma and F. Izumi, *J. Appl. Crystallogr.*, 2008, **41**, 653–658.
71 L. Shepard, A. Borisevich, T. Wang, J. Ock, A. Sokolov, C. Chen, S. Dai and S. Sinnott, Dataset for Structural Effects of Composition Tuning in A-Site Disordered Perovskite La0.5M0.5TiO3 (M = Li, Na, K) Nanorods for Solid Composite Electrolyte Design, *Zenodo*, 2025, DOI: 10.5281/zenodo.15724281.